



Diving into the interface-mediated Mars-van Krevelen (M–vK) characteristic of CuO_x-supported CeO₂ catalysts

Tian Tang^{a,b}, Lyumeng Ye^c, Yanrong Chen^{a,b}, Jingyu Xue^{a,b}, Xiaoqiang Shen^{a,b}, Jinfei Chen^{a,b}, Fiona Hammond Quarcoo^d, Vladislav Rac^e, Vesna Rakić^e, Xinbao Li^f, Xuesen Du^{a,b,*}

^a Key Laboratory of Low-Grade Energy Utilization Technologies and Systems, Ministry of Education of PRC, Chongqing University, Chongqing 400044, China

^b School of Energy and Power Engineering, Chongqing University, Chongqing 400044, China

^c Guangdong Province Engineering Laboratory for Air Pollution Control, South China Institute of Environmental Sciences, the Ministry of Ecology and Environment of PRC, Guangzhou 510655, China

^d State Key Laboratory of Materials-Oriented Chemical Engineering, College of Chemical Engineering, Nanjing Tech University, Nanjing 211816, China

^e Faculty of Agriculture, University of Belgrade, Nemanjina 6, Zemun-Belgrade 11080, Serbia

^f College of Metrology and Measurement Engineering, China Jiliang University, Hangzhou 310018, China

ARTICLE INFO

Keywords:

Copper–ceria interface

DFT+U

CO oxidation

Mars-van Krevelen (M–vK)

ABSTRACT

The unique interface synergistic catalytic properties for metal oxide-supported catalysts have long been explored in several critical heterogeneous catalytic processes (e.g., CO oxidation reactions). However, interfacial synergistic catalysis is still a hitherto undescribed mechanism due to the lack of direct evidence at the atomic level. Thereinto, the CuO_x-supported CeO₂ (CuO_x/CeO₂) catalyst is a typical case. Herein, a combination study including representative theoretical calculations, in situ DRIFTS spectra and tailored molecular probe experiments supports a new carbonate-interface mediated Mars-van Krevelen (M–vK) mechanism for CO oxidation, i.e., CO molecules form carbonate intermediate species directly between spatial proximity (2.99 Å) double lattice oxygen sites with low oxygen vacancies formation energy ($E_{\text{formO}_v} = 0.82 \text{ eV}/0.83 \text{ eV}$) at the copper–ceria interface. The reaction energy barrier of this process is 0.32 eV, much lower than the 1.23 eV of the conventional M–vK mechanism. Besides, the spatial effect of double oxygen vacancies (O_v) generated by the depletion of intermediate carbonate species promotes the sustained and dynamic activation of O₂, hence facilitating the efficient operation of the M–vK mechanism at low temperatures.

1. Introduction

The CO oxidation reaction ($\text{CO} + 1/2 \text{O}_2 = \text{CO}_2$) is a well-known model reaction to explore the relationship between structure and catalytic performance as well as a crucial process to resolve environmental pollution derived from many origins, such as automobile exhaust, hydrogen fuel cell applications, etc. [1,2]. Metal oxide cluster-supported reducible oxides with abundant metal oxide-support interfaces have proven successful in low-temperature catalysis [3,4]. Among these, CuO_x/CeO₂ catalysts have gained significant attention due to their promising potential as alternatives for noble metals in many critical environmental heterogeneous catalytic processes, including low-temperature CO oxidation, water-gas shift reaction (WGS), oxidation of volatile organic compounds (VOCs), selective catalytic reduction

of NO_x with CO (CO-SCR), etc. [5,6]. In the past decades, the strong correlation between the particle size of CuO_x supported on CeO₂ and reaction rates reported in numerous experiments studies [7–10] have powerfully confirmed the unique interfacial synergistic catalytic properties at the copper–ceria interface, which can be understood by a simple anaerobic carrier (e.g., g-C₃N₄) replacement experiment (Fig. S1). Most often, the natural active sites are attributed to the bicomponent formed on the interface between copper and ceria for CuO_x/CeO₂ catalysts. However, identifying the actual structure of such active sites on the interface is much less known, despite the catalytic reactivity or selectivity being strongly affected by metal oxide-support interactions [11].

Recently, the rapid developments in the in situ characterization and computational chemistry field provided new horizons for interface

* Correspondence to: School of Energy and Power Engineering, Chongqing University, No.174 Shazhengjie, Shapingba, Chongqing 400044, China.

E-mail address: xuesendu@cqu.edu.cn (X. Du).

<https://doi.org/10.1016/j.apcatb.2023.123368>

Received 12 July 2023; Received in revised form 2 October 2023; Accepted 6 October 2023

Available online 6 October 2023

0926-3373/© 2023 Elsevier B.V. All rights reserved.

synergistic catalytic study. Chen et al. and co-workers [12] identified the active sites of WGS reaction at the copper–ceria interfaces by in situ DRIFTS spectroscopy combined with aberration-corrected scanning transmission electron microscopy (STEM). Their results showed more intuitively than ever before that the reaction occurs at the copper–ceria interfacial perimeter, although no specific reaction mechanism was obtained at the interface. In the study of the hydrogenation of CO₂ and CO, Zhu et al. [13] further emphasized the role of the copper surface and interface sites between copper and ceria with a proposed possible reaction mechanism at the interface based on the information of intermediates from DRIFTS. However, the spatial location of intermediate species formation on the catalyst surface in DRIFTS remained elusive because of a lack of a direct quantitative correlation between infrared and kinetic measurements [14]. As a result, more researchers are combining in situ spectroscopy with computational chemistry, as theoretical calculations create an excellent platform for simulating the spatial sites of simple supported catalysts. This benefit has largely demonstrated the vital role of the metal-support interface in Pd/Au/Pt-supported CeO₂ nanoparticles in catalysis [15–17]. However, unlike Pd/Au/Pt loaded CeO₂ catalysts, this lack of data for Cu, a much cheaper metal, primarily results from the difficulties in precisely controlling the size of copper nanoparticles on ceria and directly identifying the copper–ceria interfacial. The strong copper–ceria interaction for constructing the metal–support interface proceeds via a unique pattern, vastly differing from the case of precious metals on a ceria substrate [12]. Copper locates mainly at the step edges, instead of the terraces, on ceria surfaces [18] to form irregular, small clusters that are very difficult to be imaged by electron microscopy because of the much lower degree of crystallinity and the relatively poor contrast between copper and cerium [19]. Therefore, more refined studies on the nature of the CuO_x/CeO₂ active sites and the copper–ceria interface synergistic catalytic mechanisms deserve to be designed, even though these studies [2, 13, 20] in different fields have made crucial contributions to the understanding of the copper–ceria interface in recent years.

Here, we report a detailed interface–mediated mechanistic insight on the CuO_x/CeO₂ catalyst toward the CO oxidation reaction with a particular focus on the redox processes occurring at low temperatures in reduction and reoxidation steps. With this aim, the molecular probe experiment was designed to examine the status of adsorption and M–vK mechanism on CuO_x/CeO₂ active sites in detail. In situ infrared spectroscopy probed the chemical bonding environments of the active sites and reactive gas molecules. Representative and tailored theoretical calculations combining microscopic processes with macroscopic experiments provided complementary insights into the interfacial charge transfer and the atomic bonding pattern, especially at the copper–ceria interface. This study sheds more light on interface-mediated CO oxidation characteristics of CuO_x/CeO₂ catalysts and expects to contribute to interface synergistic catalytic advancement.

2. Materials and Methods

2.1. Catalyst Preparation and Characterization

CeO₂ supports were synthesized via the reported hydrothermal method [21], and details can be found in Supporting Information. For the synthesis of 5 wt% CuO_x/CeO₂ samples, 2 g of the above CeO₂ supports and 1.66 mmol Cu(NO₃)₂·3 H₂O (99.99%, Aladdin) were dissolved in 30 mL deionized water. The mixture was evaporated by hydrothermal treatment at 80 °C for 6 h. The obtained precipitate was dried at 120 °C overnight and calcined at 500 °C in still air for 3 h at a heating rate of 5 °C/min.

Details of catalyst characterization are summarized in the Supporting Information.

2.2. Catalytic Performance Evaluation

CO catalytic oxidation and CO reaction with molecular probe (NO, NO₂) was implemented by a fixed bed using 0.2 g catalysts with the weight hourly space speed (WHSV) of 150000 mL·h^{−1}·g^{−1} at 100–500 °C. The reaction gases are typically composed of 0.5% CO, 10% O₂ (when used), 0.5% NO (when used), 0.5% NO₂ (when used), and the balance N₂ was used to simulate the flue gas. The total gas flow rate was set to 500 mL/min. Inlet and outlet gas concentrations were detected by a flue gas analyzer (SAUERMAN SI-CA130, France). The calculation details of the CO conversion, reaction rates, and turnover frequency (TOF) based on surface Cu content from ICP-OES, XPS, and EDS results (Table S1, Fig. S2, and Fig. S3) are listed in the Supporting Information.

2.3. Computational details

Spin-polarized first-principles calculations based on density functional theory (DFT) implemented in the Vienna ab initio software package (VASP) are performed with a plane-wave kinetic energy cutoff of 450 eV based on cut-off energy test results (Fig. S4). The projector-augmented wave (PAW) pseudopotentials are utilized to describe the valence-core interactions. The exchange-correlated term is defined utilizing the generalized gradient approximation (GGA) of Perdew-Burke-Ernzerhoff (PBE) with vdW correction by the DFT-D3 approach. The PBE+U approach is also used to address the on-site Coulomb interactions in the localized f/d orbitals of ceria and copper cations through an additional Hubbard-type U term for Ce 4f ($U_{\text{eff}} = 7.0$ eV) and Cu 3d state ($U_{\text{eff}} = 7.0$ eV) to correct the electron localization. The choice of this U_{eff} value is based on the satisfactory results obtained for a wide range of reactions catalyzed by ceria and copper [22–24]. The structures of the transition state (TS) for the elementary steps are obtained using the climbing image nudged-elastic band (CI-NEB) method in Transition State Tools for VASP (VTST). A set of 6 images are inserted between the initial and final state for transition state searching, which is enough to find the transition state. All the transition states in this study are confirmed with one imaginary frequency. The force and energy convergence criteria are set to 0.02 eV/Å^{−1} and 10^{−5} eV, respectively.

The equilibrium lattice constant for the CeO₂ bulk oxides is optimized based on XRD Rietveld results (Fig. 1a). The exposed CeO₂ (111) surface found by XRD and TEM is modeled by a three-layer p (3 × 3) slab separated by 15 Å vacuum in the Z direction utilizing a 6 × 6 × 1 kpoint mesh for Brillouin integration. The reliability of the kpoint mesh can be verified by Fig. S5. The bottom atom is fixed, and the two surface layers are relaxed to simulate the state of the actual surface. Moreover, the ab initio molecular dynamics (AIMD) simulation [25, 26] with a canonical ensemble is performed using the algorithm of Nöse, and the system's temperature is maintained at 400 K. The time step is set to 3 fs, and the total simulation time lasted 10 ps. Please see the Supporting Information for more details on the calculation of the Gaussian 09 program, formation energy, cohesive energy, adsorption energy, activation energy, and d band center.

3. Results and Discussion

3.1. Morphological and Structural Analysis

The physicochemical properties of the as-prepared catalysts are provided in Table S1. The elemental analysis demonstrated that all the samples containing the copper loadings were close to the target value of 5 wt%. The as-prepared CuO_x/CeO₂ catalysts presented a surface area of 23.12 m²·g^{−1}, which increased to 24.36 m²·g^{−1} after loading with CuO_x and exhibited an average pore size of ~ 10.96 nm (Fig. S6 and Table S1). The dispersion state of each element on the CuO_x/CeO₂ catalysts was examined by EDS mapping (Fig. S7a–d). The reduction ability of CuO_x/CeO₂ catalysts was identified by H₂-TPR (Fig. S8). The Rietveld refinement of the XRD spectra was used to analyze the exact change in

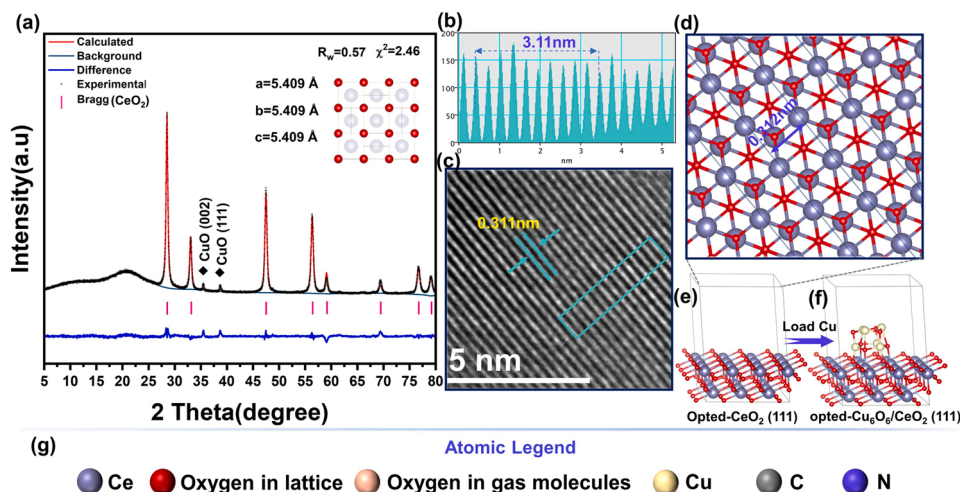


Fig. 1. (a) XRD Rietveld results of $\text{CuO}_x/\text{CeO}_2$ catalysts. (b) The measurement results of crystal plane spacing in the rectangular area of (c) by Digital Micrograph software. (c) HR-TEM images of $\text{CuO}_x/\text{CeO}_2$ catalysts in 5 nm. (d) The crystal plane spacing of (111) of CeO_2 in XRD standard card (PDF#34-0349). (e) The optimized $\text{CeO}_2(111)$ surface model. (f) The optimized $\text{Cu}_6\text{O}_6/\text{CeO}_2(111)$ surface model. (g) The legend of all atoms involved in figures.

lattice parameters. Based on XRD Rietveld results (Fig. 1a), the actual lattice constant of CeO_2 for $\text{CuO}_x/\text{CeO}_2$ was refined at 5.409 Å, which was greater than the pure CeO_2 (5.408 Å), indicating that copper atoms with smaller atomic diameter did not tend to displace cerium atoms in CeO_2 lattice, which was consistent with previous reports [9,27,28]. The grain size of the synthesized CeO_2 was initially estimated to be ~ 36 nm by Scherrer equation, and further evaluation by SEM (Fig. S9) and HR-TEM resulted in ~ 32 nm according to the exposed plane spacing of 0.311 nm (Fig. 1b, c) for $\text{CeO}_2(111)$, which was within the permissible error range. The above results on the catalyst structure and surface state provided a more precise direction for theoretically computational

modeling (Fig. 1e, f).

The typical fluorite structure of ceria and the weak and broad characteristic diffraction peaks attributed to $\text{CuO}(002)$ and $\text{CuO}(111)$ planes were detected in XRD patterns (Fig. S10); as expected, Cu existed mainly as poorly crystalline CuO clusters (~ 8 nm) on the surface of CeO_2 (Fig. 2a-c). The original cells of CeO_2 were constructed and optimized by XRD Rietveld results since it was more compatible with the actual catalysts. The stable exposed (111) plane in XRD and HR-TEM was cleaved for model support, and the (111) was also the most reported crystal plane for theoretical calculations of ceria. The formation energy calculations (Fig. 2d) of Cu_nO_n clusters on the $\text{CeO}_2(111)$ surface

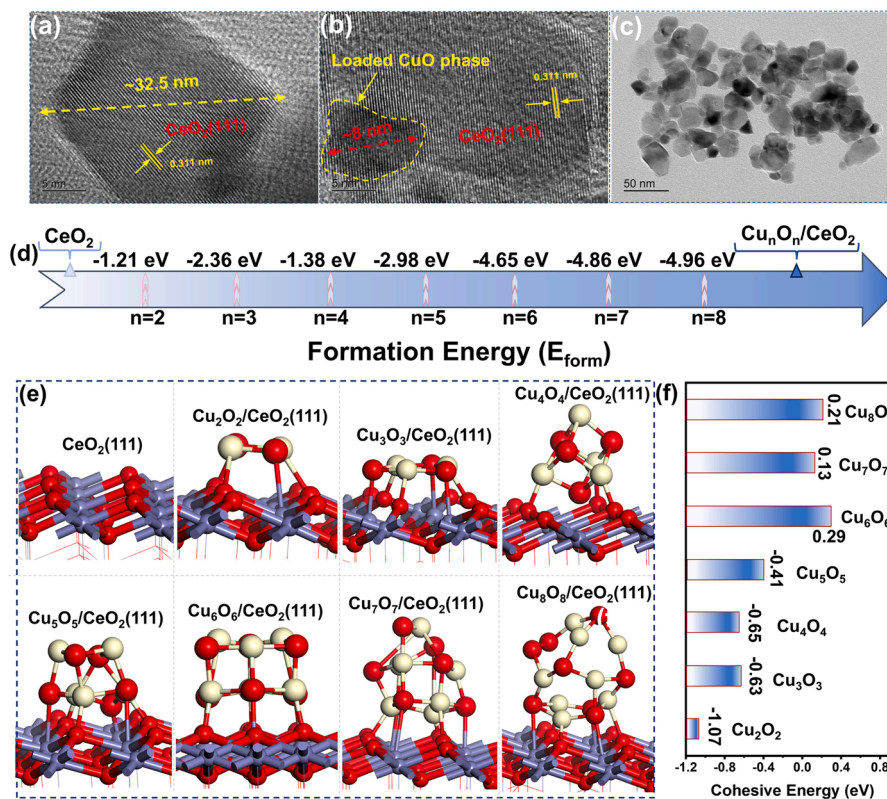


Fig. 2. (a-c) HR-TEM images of $\text{CuO}_x/\text{CeO}_2$ catalysts in 5 nm, 5 nm, and 50 nm. (d) Calculated formation energy of Cu_nO_n clusters on $\text{CeO}_2(111)$ surface. (e) The optimized structures of Cu_nO_n clusters on $\text{CeO}_2(111)$. (f) Calculated cohesive energy of Cu_nO_n clusters.

were utilized to evaluate the stability of species $\text{Cu}_n\text{O}_n/\text{CeO}_2(111)$. Combining the above observed relative grain sizes of Cu and Ce, the metal oxide clusters of Cu_nO_n ($n = 2-8$) were constructed to simulate the copper species state on the CeO_2 surface because it is not realistic to generate a sufficient number of potential configurations manually in this stage [27]. The formation energy of $\text{Cu}_n\text{O}_n/\text{CeO}_2(111)$ showed an abrupt increase when $n = 6$ (-4.65 eV), but the increment was suppressed after $n > 6$ (Fig. S11), which might be jointly determined by the structure symmetry and the inter-atomic contacting area after the relaxation of $\text{Cu}_6\text{O}_6/\text{CeO}_2(111)$ (Fig. 2e).

The cohesive energy for isolated CuO_x clusters with different sizes gives an indication of the average Cu–O–Cu bond strength [29]. The cohesive energy for Cu_nO_n clusters with different sizes was calculated and displayed in Fig. 2(f). The cohesive energy increased significantly with the increasing Cu_nO_n cluster size from $n = 2$ (-1.07 eV) to 6 (0.29 eV). For larger clusters with Cu_7O_7 and Cu_8O_8 , the cohesive energies decreased due to the poor symmetry of the optimized conformation. These results demonstrated stronger Cu–O–Cu bonding in isolated Cu_6O_6 clusters with high symmetry. Besides, the AIMD result (Fig. S12) of up to 10 ps at 400 K also fully confirmed the structural stability of $\text{Cu}_6\text{O}_6/\text{CeO}_2(111)$. Based on the above discussion, the $\text{Cu}_6\text{O}_6/\text{CeO}_2(111)$ surface model with a relatively stable structure was a more representative calculation model under the current arithmetic. Still, a more stable structure on a larger surface model could not be excluded because this was beyond most of the current computer arithmetic.

3.2. Active Site Analysis

The representativeness of the theoretical model to the actual catalyst directly determines the reliability of the calculated results and usually tends to be ignored. Here, we performed detailed calculations to predict the active sites of $\text{Cu}_6\text{O}_6/\text{CeO}_2(111)$ with different adsorption probe molecules (CO , O_2 , NO , NO_2), and the exact location of the active sites could be obtained in Fig. S13. The adsorption energy of adsorbed probe molecules at different active sites was calculated in Fig. 3(a). As depicted in Fig. 3(a), the surface Cu^{2+} site ($\text{CuCe}(\text{Cu}_{\text{sur}}^{2+})$) was the best adsorption site for CO molecules with a moderate strength of adsorption energy ($E_{\text{ads}} = -0.99$ eV). Notably, O_2 , NO , and NO_2 molecules also exhibited excellent exothermic adsorption on the Cu^{2+} surface, and NO_2 ($E_{\text{ads}} = -1.53$ eV) $>$ NO ($E_{\text{ads}} = -1.42$ eV) $>$ O_2 ($E_{\text{ads}} = -1.34$ eV). These results implied a substantial competitive adsorption property of the probe molecule on the $\text{CuCe}(\text{Cu}_{\text{sur}}^{2+})$ site.

Oxygen vacancy formation energy (E_{formO_v}) is widely recognized as a descriptor for CO oxidation reactions in loaded metal oxide cluster catalysts [30–32]. In this sense, the formation of oxygen vacancy on the surface of $\text{CeO}_2(111)$ and $\text{Cu}_6\text{O}_6/\text{CeO}_2(111)$ was systematically

examined by the calculation of E_{formO_v} . The location, naming, and calculation results of oxygen vacancies are presented in Fig. S14. The pure $\text{CeO}_2(111)$ surface oxygen vacancy formation energy was endothermal 4.24 eV, a higher value as reported in the literature [33], indicating that the separation of an oxygen atom from the stable $\text{CeO}_2(111)$ was costly. Specifically, the double spatially proximity (2.99 Å) lattice oxygen vacancies ($\text{CuCe-Ce}(\text{O}_v)_{\text{near}}/\text{CuCe-Cu}(\text{O}_v)_{\text{int}}$) at the copper–ceria interface exhibited extremely low oxygen vacancies formation energy ($E_{\text{formO}_v} = 0.83$ eV/0.82 eV) on $\text{Cu}_6\text{O}_6/\text{CeO}_2(111)$, suggesting that the formation of $\text{CuCe-Ce}(\text{O}_v)_{\text{near}}$ and $\text{CuCe-Cu}(\text{O}_v)_{\text{int}}$ was energetically favorable. Hence the two more active lattice oxygen sites will preferentially participate in the M–vK process of CO oxidation. Additionally, we utilized molecular probes with different oxidation properties (NO , NO_2 , and O_2) re-adsorbed on oxygen vacancies to simulate the oxidation process of oxygen vacancies and further investigated the reoxidation capacity of oxygen vacancies. The correlation between the oxygen vacancy formation energy for different lattice oxygen sites and the adsorption energy for the probe molecule is shown in Fig. 3(b) and Table S2. The more easily formed oxygen vacancies correspond to a weaker reoxidation capacity, well reflected in the excellent fitting determined by the stability of oxygen vacancies [34]. Notably, the results of the adsorption capacity for different oxidant probe molecules at oxygen vacancies implied that NO_2 is a significantly better oxidant than NO and O_2 for the reoxidation of oxygen vacancies, which is consistent with our previous work [35,36].

The bond lengths (calculated/actual = 1.126 Å/ 1.128 Å), energy band structures, and valence orbitals of CO molecules were fully simulated by VASP and Gaussian 09 program, and the simulation results were almost identical to the actual or standard results (Fig. 4a). The surface Cu^{2+} moved to the lower valence state, accompanied by the transfer of electrons on CO to Cu, which could be fully demonstrated by the shift of the d-band center (-3.71 eV \rightarrow -3.59 eV) of Cu to the Fermi energy level after the adsorption of CO molecules (Fig. 4b).

The effect of Cu_6O_6 clusters on $\text{CeO}_2(111)$ was analyzed in-depth by combining crystal field multiplet theory and molecular orbital theory. As seen in Fig. 4(b), there was a significant left shift in the non-occupied state of $\text{Cu}_6\text{O}_6/\text{CeO}_2(111)$ compared to $\text{CeO}_2(111)$, suggesting a decrease in the energy of the unoccupied state of $\text{CeO}_2(111)$, accompanied by the transfer of electrons on $\text{CeO}_2(111)$ to the Cu_6O_6 cluster, which was well confirmed by the differential charge density result (Fig. 6d) and the apparent reduction of Ce^{3+} species in XPS (Fig. 6e). Fig. 4(c) illustrated the energy level of 3d orbitals (from Fig. 4d), uncovering key differences in the 3d orbital sequence for $\text{Cu}_6\text{O}_6/\text{CeO}_2(111)$ and Cu_6O_6 clusters. To eliminate the degeneracy, the 3d orbitals of Cu atoms split into two orbitals, t_{2g} and e_g . The Jahn-Teller effect of $\text{Cu}_6\text{O}_6/\text{CeO}_2(111)$ was significantly lower than that of Cu_6O_6

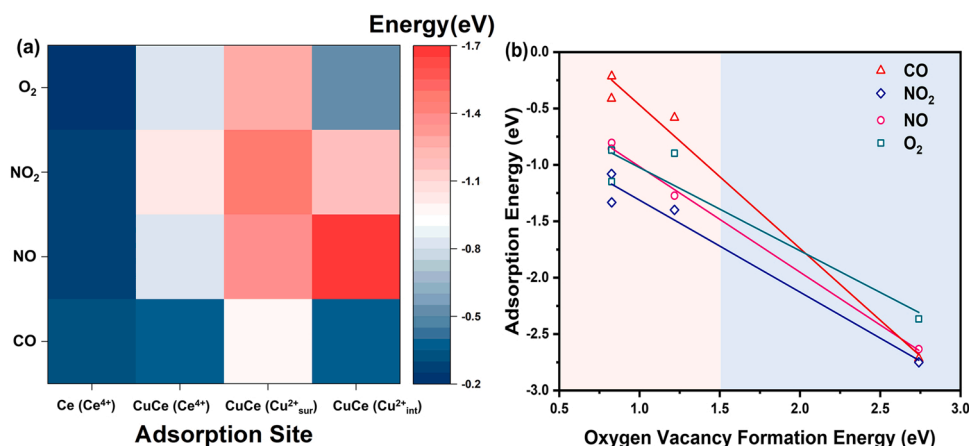


Fig. 3. (a) Probe molecule adsorption energy at different active sites. (b) The correlation between the oxygen vacancy formation energy for different lattice oxygen sites and the adsorption energy for different probe molecules.

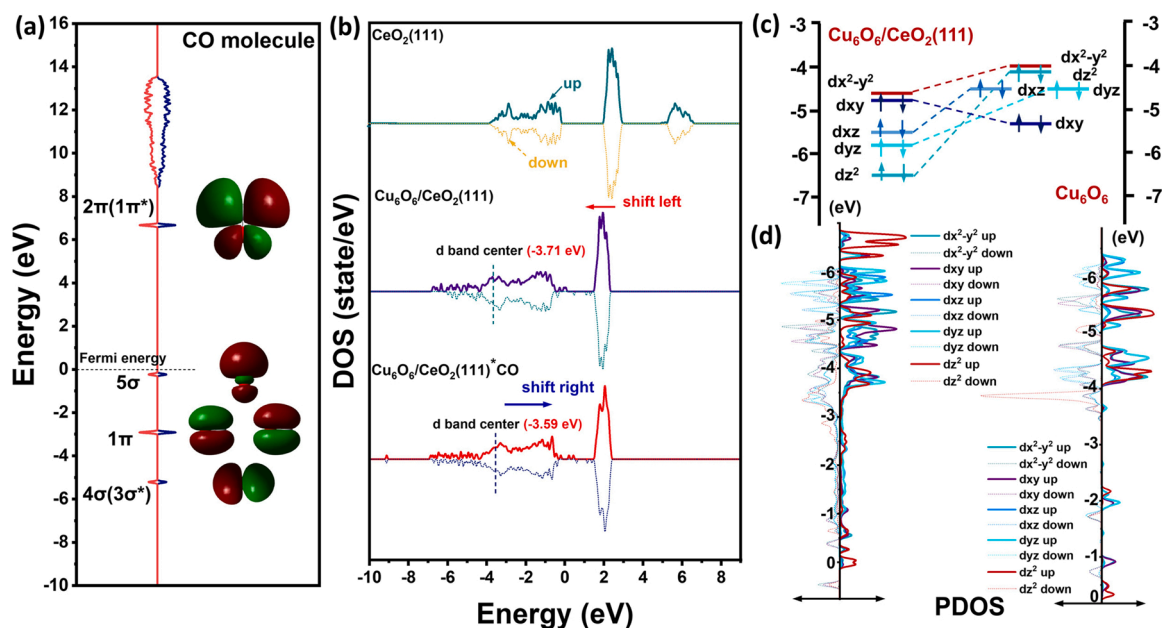


Fig. 4. (a) Valence orbitals and corresponding energy of CO molecules. (b) DOS for $\text{CeO}_2(111)$, $\text{Cu}_6\text{O}_6/\text{CeO}_2(111)$, and CO adsorbed on $\text{Cu}_6\text{O}_6/\text{CeO}_2(111)$ surface. (c) Cu 3d orbital splitting of Cu centers in $\text{Cu}_6\text{O}_6/\text{CeO}_2(111)$ and Cu_6O_6 cluster. (d) 3d orbital-resolved DOS for Cu in $\text{Cu}_6\text{O}_6/\text{CeO}_2(111)$ and Cu_6O_6 cluster.

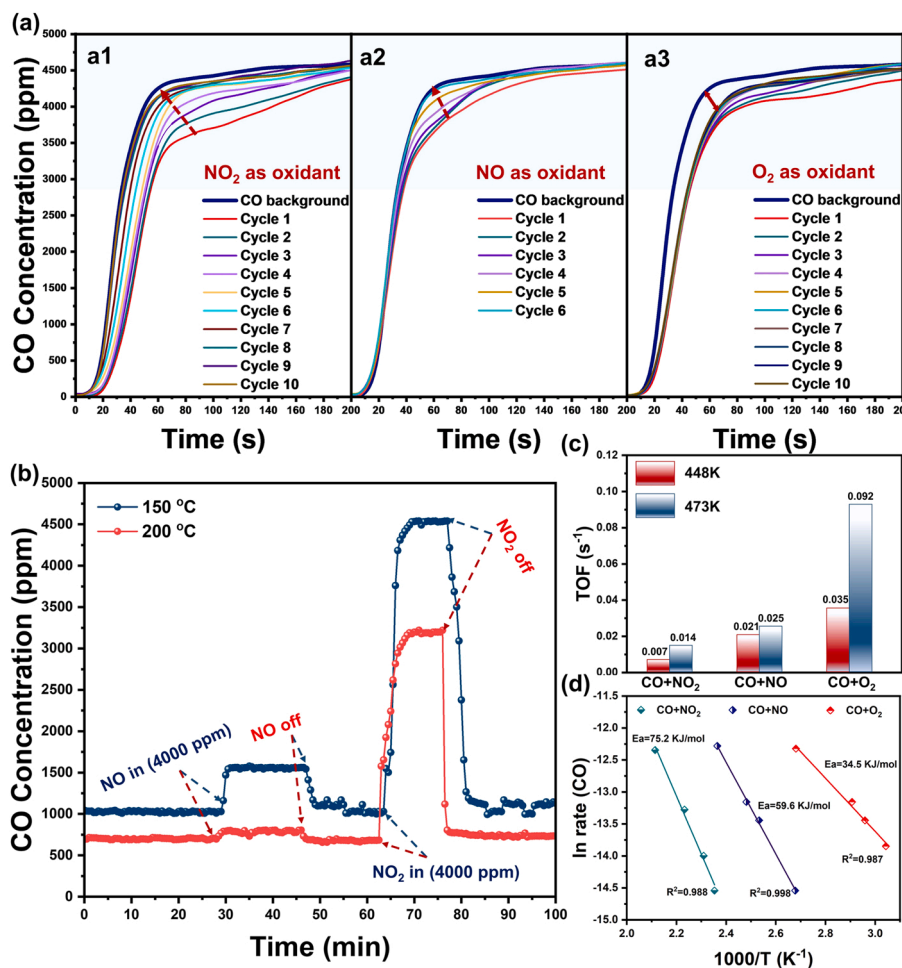


Fig. 5. (a) The results of the molecular probe experiment, a1, a2, and a3 correspond to NO_2 , NO, and O_2 as oxidants, respectively. (b) The results of NO and NO_2 transient probe injection experiment during the CO oxidation at 150 °C and 200 °C, respectively. (c) TOF of $\text{CO}+\text{NO}_2$, $\text{CO}+\text{NO}$, and $\text{CO}+\text{O}_2$ reaction over $\text{CuO}_x/\text{CeO}_2$ catalysts at 448 K and 473 K, respectively. (d) Arrhenius plots obtained by reaction rate at different temperatures.

clusters, indicating $\text{Cu}_6\text{O}_6/\text{CeO}_2(111)$ brings more d-band active electrons near the Fermi energy level [37]. Most notably, a decline of dx^2-y^2 , dz^2 , dxz , and dyz , along with a rise of dxy was observed from Cu_6O_6 clusters to $\text{Cu}_6\text{O}_6/\text{CeO}_2(111)$. It is understood that the weakened repulsive force between ligand and electrons in the z direction upon axial coordination results in the elevation of d-orbital energy levels containing z ingredients [38], also explaining the blue-shift phenomenon accompanying the CuO_x loading in the FTIR spectral results (Fig. S15). Such a displacement decreases the antibonding interaction in the z direction, so the energy level of the dz^2 orbital was significantly reduced, making $\text{Cu}_6\text{O}_6/\text{CeO}_2(111)$ stronger electrophile and facilitating binding to Lewis base-like CO.

3.3. Molecular Probe Experimental and Catalytic Kinetic Studies

Simultaneously, a transient probe molecular injection experiment was designed during the CO oxidation at 150 °C and 200 °C, respectively, as shown in Fig. 5(b). The injection of 0.5% NO or 0.5% NO_2 reduced the CO oxidation performance to different degrees. However, this phenomenon was fully recovered after the cut-off of NO or NO_2 , displaying a typical competitive adsorption process as predicted by the theoretical calculations above. The injection of NO_2 obviously exhibited more inhibitory effect for CO oxidation than NO, attributed to the stronger affinity of the $\text{CuCe}(\text{Cu}_{\text{sur}}^{2+})$ site for NO_2 and the separation of NO adsorption sites, since the interface Cu^{2+} site ($\text{CuCe}(\text{Cu}_{\text{int}}^{2+})$) exhibited the higher adsorption energy ($E_{\text{ads}} = -1.75$ eV) for NO. The DRIFTS spectrum of separate NO adsorption and CO+NO co-adsorption is shown in Fig. S16, and the assignment of peaks is identified in Table S3. It could be clearly seen that the carbonate and nitrate species generated by CO and NO co-adsorption exhibited similar characteristic peak intensities, which also supported the separation of the CO and NO adsorption sites.

It is worth mentioning that O_2 is always available on the catalysts surface since oxygen is in excess, and the competitive adsorption of oxygen can be ignored. The well-predicted results of the different adsorption molecular calculations for the injection experiments provided robust evidence for further active site analysis.

Cyclic oxidation of oxygen vacancies determines the continued operation of the M–vK mechanism. For this purpose, we designed a molecular probe (NO_2 , NO, and O_2) cycle experiment attempting to investigate the CO oxidation characteristic of the interface-mediated M–vK mechanism for $\text{CuO}_x/\text{CeO}_2$, since isotopic labeling and DRIFTS could not capture the intensity of the M–vK process. For the molecular probe cycle experiment, the $\text{CuO}_x/\text{CeO}_2$ catalyst was reduced at 200 °C for 20 min using 20% CO/N_2 . The generated oxygen vacancies on the $\text{CuO}_x/\text{CeO}_2$ surface after reduction could be proved by the significant increase in Cu^+ content (Fig. 6b and Table S4), the decrease in surface lattice oxygen content (Fig. S17 and Table S4) in the XPS results, and the enhanced symmetrical EPR signal ($g = 2.003$) originated from the unpaired electrons at oxygen vacancy sites (Fig. 6c). The response curve of CO was measured online by a flue gas analyzer as the response background curve of CO (line "CO background" in Fig. 5a) by continuously feeding 0.5% CO to the above reduced $\text{CuO}_x/\text{CeO}_2$ catalyst. Then, the different molecular probes (NO_2 , NO, and O_2) were used to reoxidize the above reduced $\text{CuO}_x/\text{CeO}_2$ catalyst. EPR and Cu 2p spectrum results clearly confirmed that even NO molecules with relatively poor oxidation properties could achieve the reoxidation of the reduced $\text{CuO}_x/\text{CeO}_2$ catalyst. After the reoxidation, 0.5% CO was introduced, and the CO response curve was measured online until the CO content stabilized (obtained line "Cycle 1" in Fig. 5a). Significantly, all reoxidation times were strictly controlled at 20 min, and each step of oxidation and reduction was followed by a 20 min N_2 purge to increase the experiment reliability. The CO reduction response curves of "Cycle 2, Cycle 3, Cycle

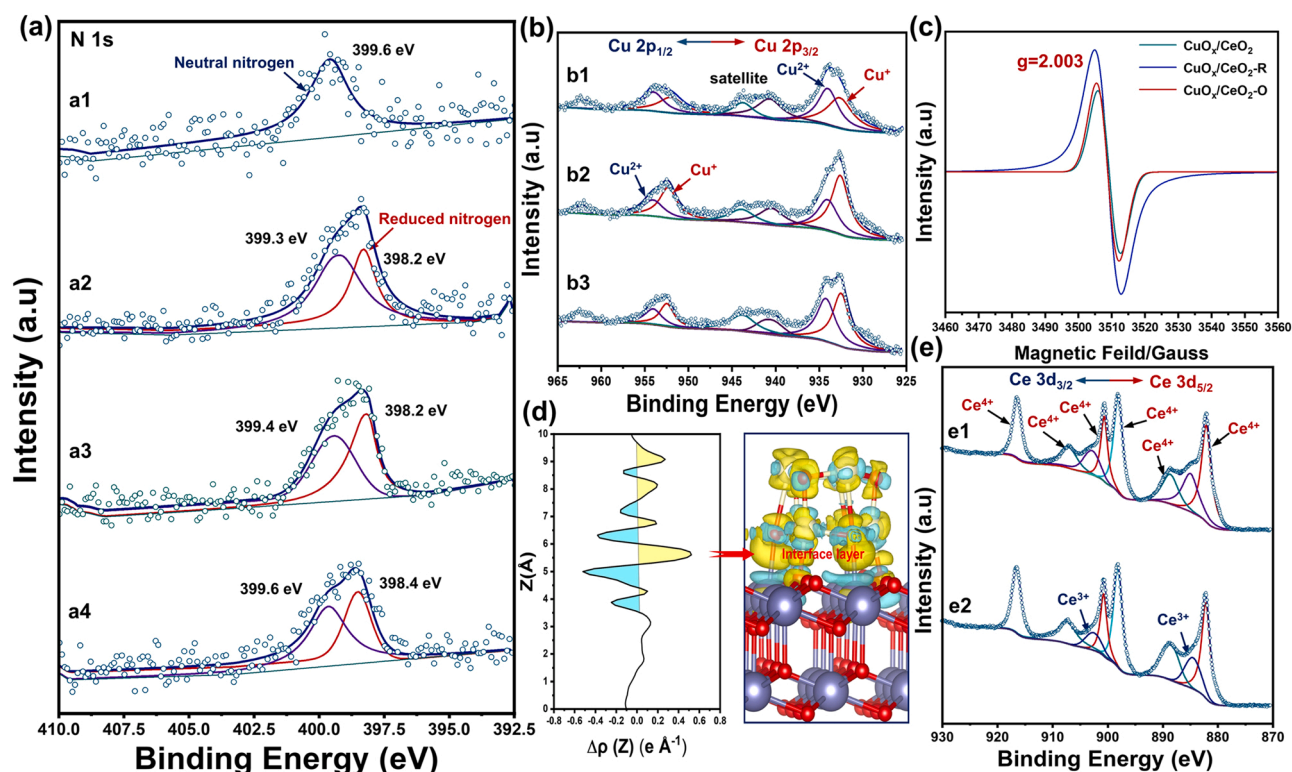


Fig. 6. (a) XPS spectra for N 1s; a1, a2, a3, a4 correspond to $\text{CuO}_x/\text{CeO}_2$, $\text{CuO}_x/\text{CeO}_2$ (Cycle 1), $\text{CuO}_x/\text{CeO}_2$ (Cycle 3), and $\text{CuO}_x/\text{CeO}_2$ (Cycle 5) catalysts using NO as oxidant, respectively, from Fig. 5a1 (more details can be found in the Table S4 notes a–c). (b) XPS spectra for Cu 2p, b1, b2, b3 correspond to $\text{CuO}_x/\text{CeO}_2$, $\text{CuO}_x/\text{CeO}_2\text{-R}$, and $\text{CuO}_x/\text{CeO}_2\text{-O}$ catalysts, respectively (more details can be found in the Table S4 notes d, e). (c) Room temperature EPR spectra of $\text{CuO}_x/\text{CeO}_2$, $\text{CuO}_x/\text{CeO}_2\text{-R}$, and $\text{CuO}_x/\text{CeO}_2\text{-O}$ (more details can be found in the Table S4 notes d, e). (d) Calculated bonding charge analysis for Cu_6O_6 cluster supported $\text{CeO}_2(111)$ surface, and the left panels represent plane-integrated bonding charge $\Delta\rho(z)$ plotted as a function of z -coordinate across the copper–ceria interface. (e) XPS spectra for Ce 3d; e1 and e2 correspond to CeO_2 and $\text{CuO}_x/\text{CeO}_2$ catalysts, respectively.

5..." were obtained by cyclic reoxidation with different probe molecules to simulate the operation of the M-vK mechanism on the $\text{CuO}_x/\text{CeO}_2$ catalyst, and the local enlarged images of Fig. 5(a) can be viewed in Fig. S18.

As seen in Fig. 5(a), the first NO_2 reoxidation CO response curve (line "Cycle 1" in Fig. 5a1) was significantly lower than that of NO (Fig. 5a2) and O_2 (Fig. 5a3), indicating that NO_2 was a better oxidizer than NO and O_2 at 200 °C for $\text{CuO}_x/\text{CeO}_2$ catalysts, which was consistent with the oxygen vacancy re-adsorbed result. However, the CO response curves of

NO and NO_2 almost coincided with the background response curves after 6 and 10 reoxidation cycles (Fig. 5a1, a2), respectively. This phenomenon was not observed with O_2 as an oxidant (Fig. 5a3), suggesting that the M-vK mechanism with NO or NO_2 as an oxidant could not operate continuously on $\text{CuO}_x/\text{CeO}_2$ catalysts, which also inadvertently revealed the reason why the generally accepted $\text{CuO}_x/\text{CeO}_2$ catalysts mainly proceed by L-H mechanism in the CO-SCR reaction from another perspective [39–41]. The $\text{CuO}_x/\text{CeO}_2$ catalysts with different cycle times (NO as oxidant) were employed for XPS to explore the

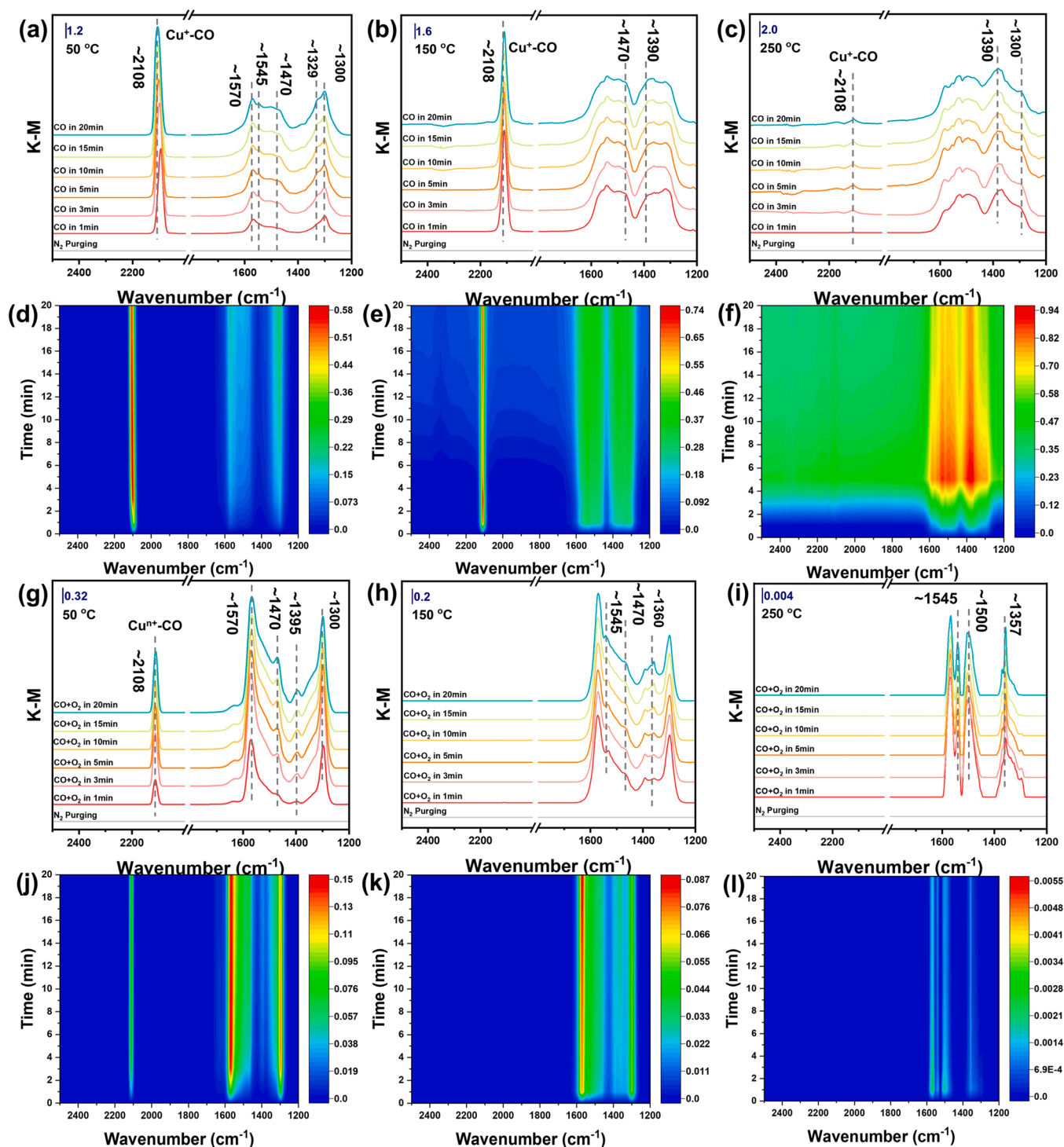


Fig. 7. (a-c) In situ DRIFTS spectra of $\text{CuO}_x/\text{CeO}_2$ catalysts for CO adsorption alone at 50 °C, 150 °C, and 200 °C, respectively. (d-f) Transformed time-resolved in-situ DRIFTS spectra for CO adsorption at 50 °C, 150 °C, and 200 °C, respectively. (g-i) In situ DRIFTS spectra of $\text{CuO}_x/\text{CeO}_2$ catalysts for CO oxidation reaction at 50 °C, 150 °C, and 200 °C, respectively. (j-l) Transformed time-resolved in-situ DRIFTS spectra for CO oxidation reaction at 50 °C, 150 °C, and 200 °C, respectively.

blocked M–vK mechanism), are shown in Fig. 6(a). Based on the split peak fitting for N1s [42], a characteristic peak attributed to the reduced nitrogen state [43,44] was detected in the catalyst after the first (cat. "cycle 1"), third (cat. "cycle 3"), and fifth (cat. "cycle 5") oxidation with NO (Fig. 6a2–a4), indicating that surface nitrogen enrichment was likely to be responsible for the blocked M–vK mechanism. For this purpose, we further calculated the adsorption energy of the N/O terminals of NO and NO₂ at the interface oxygen vacancies (CuCe–Cu (O_v)_{int}) in Fig. S19. The significantly stronger oxygen vacancy N-terminal adsorption capacity of NO corresponds to fewer cycles. Combined with XPS results, it could be reasonably inferred that the blocked M–vK mechanism was caused by nitrogen coverage of surface oxygen vacancies, and a recent study [45] also supports the possibility. Therefore, the continuous operation of the M–vK mechanism on the surface of CuO_x/CeO₂ catalysts exhibits oxidant-dependent properties, i.e., the recycling of oxygen vacancies on the surface of the CuO_x/CeO₂ catalyst requires the O atoms for replenishment, not N atoms.

Hence, the CO-SCR (CO+NO/CO+NO₂) and CO oxidation reactions were further designed for a comparative study of the effect of the M–vK mechanism involvement on the catalytic activity, as shown in Fig. S20. Fig. 5(c) and Fig. 5(d) depicted the results of the turnover frequency (TOF) and apparent activation energy (*E_a*) tests. Impressively, the apparent activation energy of CO oxidation (~34.5 kJ/mol) was significantly lower than that of CO+NO (~59.6 kJ/mol) or CO+NO₂ (~75.2 kJ/mol), and the TOF of CO oxidation was 3–4 times higher than the CO+NO reaction at 200 °C, and even though their conversion rates did not differ by more than 15% (Fig. S20). Based on the above discussion of the active sites and the M–vK mechanism, it is evident that the interface-mediated M–vK mechanism played a crucial role in CO oxidation for CuO_x/CeO₂ catalysts.

3.4. In situ DRIFTS Analysis and Reaction Mechanism of CO Catalytic Oxidation

The mechanism of CO catalytic oxidation on CuO_x/CeO₂ catalysts is revealed by in situ DRIFTS. The separate CO adsorption is used to identify the peaks (Fig. 7a–f), and the CO and O₂ co-adsorption spectra at different temperatures are shown in Fig. 7(g–l). A strong band of Cu⁺–CO species was discerned at ~2108 cm^{−1}, indicating that CO mainly adsorbs on Cu²⁺ sites and forms Cu⁺–CO species after its electron interaction with CuO_x/CeO₂ [20], consistent with the results of the DFT calculation. For the separate CO adsorption, the bidentate carbonates (~1570 and ~1300 cm^{−1}) were the most prominent intermediate species, accompanied by a few bridge carbonates (~1545 and ~1500 cm^{−1}) and mono-/tridentate carbonates (1350–1400 cm^{−1} and 1470 cm^{−1}) [20,46–50], and the intensity of these carbonate species showed a significant increasing trend with the increase in temperature (Fig. 7d–f). Notably, the increased enhancement of monodentate carbonate species was more pronounced, indicating that the extraction of lattice oxygen by CO was further enhanced with increasing temperature. These results also indirectly demonstrate the activation of the M–vK mechanism. In addition, the Cu⁺–CO species disappeared completely at 250 °C and was accompanied by a higher signal-to-noise ratio (Fig. 7c, f), indicating that the desorption rate of the CO sustained adsorption process was significantly faster than the adsorption rate at 250 °C, which was also well corroborated by the CO-TPD results (Fig. S21). However, when switching the atmosphere to CO+O₂, the peaks of Cu⁺–CO and carbonate species were significantly decreased at 50 °C (Fig. 7g, j), combined with the ignition temperature in the catalyst activity test results, which could be attributed to the competition of O₂ for CO adsorption sites rather than to the depletion of CO. Furthermore, no CO₂ adsorption peaks were observed in 2300–2400 cm^{−1} [51], while that peaks of carbonate species showed a significant decrease (Fig. 7h, k) at 150 °C, and almost completely disappeared (Fig. 7i, l) at 250 °C (normalized intensity 0.004), suggesting that the desorption of CO₂ was easy and the decomposition and consumption of carbonate species

played a vital role in CO oxidation, as it was accompanied by an obvious increase in catalytic activity, also generally accepted in recent literature [52–54].

Liu et al. and co-workers [55] pioneered a carbonate-mediated M–vK mechanism by purely theoretical calculations in the cobalt-doped ceria CO oxidation system. Unfortunately, to be practical and realistic, due to the lack of experimental support and representative models, the calculated results were not well applicable to metal oxide-supported CeO₂ catalysts since the simple metal substitution doping model ignored the spatial effect between the metal oxide–support interface. Nevertheless, inspired by this pioneering work, we constructed the M–vK reaction path with carbonate participation at the copper–ceria interface of CuO_x/CeO₂ catalysts for the first time based on the above representative experiments and theoretical calculations. Fig. 8 and Fig. 9 present the energetic information and optimized structure of the conventional M–vK, together with the carbonate interface-mediated M–vK mechanism. The pathway setting and active site selection were based on the discussion above. For the conventional M–vK process, i.e., the first CO molecule adsorbs (a–b), lattice oxygen was captured by CO to generate CO₂ (b–c), the first CO₂ desorption (c–d), lattice oxygen was replenished by O₂ (d–e), the second CO molecule adsorbs (e–f), CO reacted with activated O to generate CO₂ (f–g), and the second CO₂ desorption (g–h).

Interestingly, unlike the traditional M–vK process, after several calculations to verify, we found that the spatial proximity (2.99 Å) double lattice oxygen sites with low oxygen vacancy formation energy (*E_{formO_v}* = 0.82 eV/0.83 eV) allowed the adsorbed CO molecules to form carbonate species directly at the copper–ceria interface and the reaction energy barrier of this process was 0.32 eV (TS), which was much lower than the 1.23 eV (TS1) of the conventional M–vK mechanism. Besides, it could be seen that the endothermic 0.3 eV for the CO₂ desorption (e–f) was thermodynamically favorable to achieve, explaining well the absence of the peak of adsorbed species in DRIFTS. In detail, the exothermic activation of O₂ is −3.16 eV (f–g') for double oxygen vacancies involved in the carbonate interface-mediated M–vK process, which was much lower than the exotherm of −1.16 eV (d–e) for the conventional M–vK process involving one oxygen vacancy. Notably, almost no transition state for oxygen dissociation was observed in the step of f–g', suggesting that the activation and dissociation of O₂ were thermodynamically very favorable with the assistance of double oxygen vacancies at the copper–ceria interface. These well-matched theoretical calculations and experimental results explained well the formation and consumption of intermediate carbonate species and the interfacial synergistic catalytic effect of CuO_x/CeO₂ catalysts in CO oxidation.

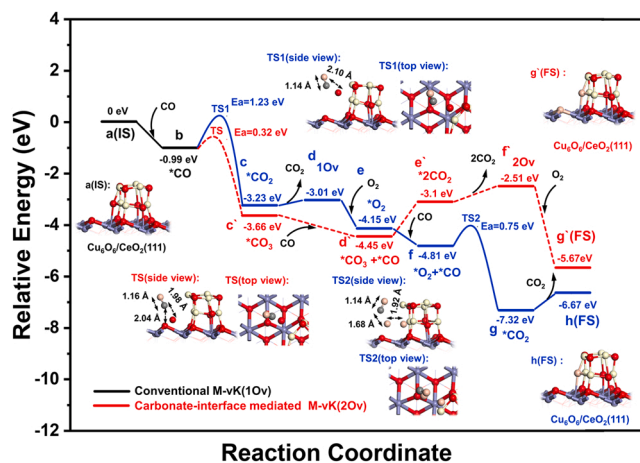


Fig. 8. The interface-mediated conventional/carbonate involved M–vK reaction path and theoretical relative energy of CuO_x/CeO₂ catalysts.

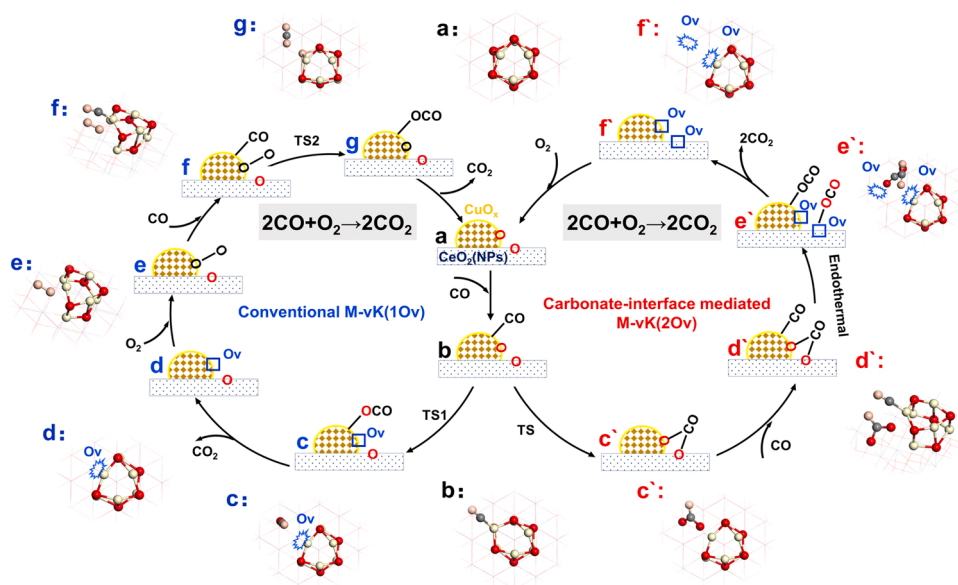


Fig. 9. Theoretical stationary structures and reaction processes of the interface-mediated conventional/carbonate involved M-vK reaction path.

4. Conclusion

In this work, the typical $\text{CuO}_x/\text{CeO}_2$ catalysts with interfacial synergistic catalytic effect were precisely synthesized. The active sites of $\text{CuO}_x/\text{CeO}_2$ and its electronic structure were examined in detail through a combination of characterization, experimental design, and representative theoretical calculations. The molecular probe experiments, oxygen vacancy formation calculations, in situ infrared spectroscopy, and kinetic tests provided insights into the M-vK mechanism of the $\text{CuO}_x/\text{CeO}_2$ catalysts. A new carbonate-interface mediated M-vK mechanism was provided for CO oxidation, clarifying the formation and consumption processes of intermediate carbonate species and the interfacial synergistic catalytic effect of $\text{CuO}_x/\text{CeO}_2$ catalysts. Another phenomenon based on molecular probe experiments and XPS results, worth mentioning was that the continuous operation of the M-vK mechanism on the surface of $\text{CuO}_x/\text{CeO}_2$ catalysts exhibited oxidant-dependent properties. The coverage of oxygen vacancies by surface nitrogen species blocked this mechanism, even though NO_2 was a significantly better oxidant than O_2 for the reoxidation of oxygen vacancies at low temperatures. This study also demonstrated the essential, but often neglected, need to regard the spatial effects at the interface of supported metal oxide catalysts to describe the interfacial synergistic catalytic mechanism.

CRedit authorship contribution statement

Tian Tang: Conceptualization, Formal analysis, Investigation, Methodology, Software, Validation, Writing – original draft, Writing – review and editing. **Lyumeng Ye :** Writing – review & editing, language editing, Resources. **Yanrong Chen :** Funding acquisition, Project administration, Resources, Supervision. **Jingyu Xue:** Validation, Date curation. **Xiaoqiang Shen:** Software, Date curation. **Jinfei Chen:** Software, Date curation. **Fiona Hammond Quarcoo:** Writing - review and editing. **Vladislav Rac:** Writing – review & editing. **Vesna Rakić:** Writing – review & editing. **Xinbao Li:** Validation, Date curation. **Xuesen Du:** Funding acquisition, Project administration, Resources, Supervision.

Declaration of Competing Interest

There are no conflicts to declare.

Data Availability

Data will be made available on request.

Acknowledgment

We gratefully acknowledge the financial support of the National Key R&D Program of China (2021YFE0110800); the National Natural Science Foundation of China (No. 52176100); Natural Science Foundation of Chongqing (cstc2021jcyj-msxmX0247), and Open Fund of Guangdong Province Engineering Laboratory for Air Pollution Control (20193236-09-02).

Appendix A. Supporting information

Supplementary data associated with this article can be found in the online version at [doi:10.1016/j.apcatb.2023.123368](https://doi.org/10.1016/j.apcatb.2023.123368).

References

- [1] W.Z. Yu, W.W. Wang, S.Q. Li, X.-P. Fu, X. Wang, K. Wu, et al., Construction of active site in a sintered copper-ceria nanorod catalyst, *J. Am. Chem. Soc.* 141 (44) (2019) 17548–17557.
- [2] A. Davo-Quinonero, E. Bailon-Garcia, S. Lopez-Rodriguez, J. Juan-Juan, D. Lozano-Castello, M. Garcia-Melchor, et al., Insights into the oxygen vacancy filling mechanism in CuO/CeO_2 catalysts: a key step toward high selectivity in preferential CO oxidation, *ACS Catal.* 10 (11) (2020) 6532–6545.
- [3] J. Kim, H. Choi, D. Kim, J.Y. Park, Operando surface studies on metal-oxide interfaces of bimetal and mixed catalysts, *ACS Catal.* 11 (14) (2021) 8645–8677.
- [4] X. Wang, T. Li, H. Wang, K. Zhao, Y. Huang, H. Yuan, et al., Identifying active sites at the Cu/Ce interface for hydrogen borrowing reactions, *J. Catal.* 418 (2023) 163–177.
- [5] Y. Fang, X. Chi, L. Li, J. Yang, S. Liu, X. Lu, et al., Elucidating the nature of the Cu(I) active site in CuO/TiO_2 for excellent low-temperature CO oxidation, *ACS Appl. Mater. Interfaces* 12 (6) (2020) 7091–7101.
- [6] M. Xu, S. Yao, D. Rao, Y. Niu, N. Liu, M. Peng, et al., Insights into interfacial synergistic catalysis over $\text{Ni}/\text{TiO}_{2-x}$ catalyst toward water-gas shift reaction, *J. Am. Chem. Soc.* 140 (36) (2018) 11241–11251.
- [7] D. Gamarra, C. Belver, M. Fernandez-Garcia, A. Martinez-Arias, Selective CO oxidation in excess H_2 over copper-ceria catalysts: Identification of active entities/species, *J. Am. Chem. Soc.* 129 (40) (2007) 12064–12065.
- [8] S.D. Senanayake, D. Stacchiola, J.A. Rodriguez, Unique properties of ceria nanoparticles supported on metals: novel inverse ceria/copper catalysts for CO oxidation and the water-gas shift reaction, *Acc. Chem. Res.* 46 (8) (2013) 1702–1711.
- [9] H. Sun, H. Wang, Z. Qu, Construction of CuO/CeO_2 catalysts via the ceria shape effect for selective catalytic oxidation of ammonia, *ACS Catal.* 13 (2) (2023) 1077–1088.

- [10] M.F. Luo, Y.P. Song, J.Q. Lu, X.Y. Wang, Z.Y. Pu, Identification of CuO species in high surface area CuO-CeO₂ catalysts and their catalytic activities for CO oxidation, *J. Phys. Chem. C* 111 (34) (2007) 12686–12692.
- [11] H. Sun, P. Zhang, J. Wang, S. Ye, J. Fu, J. Zheng, et al., Understanding the suppressive role of catalytically active Pt-TiO₂ interfacial sites of supported metal catalysts towards complete oxidation of toluene, *J. Mater. Chem. A* 10 (48) (2022) 25633–25643.
- [12] A. Chen, X. Yu, Y. Zhou, S. Miao, Y. Li, S. Kuld, et al., Structure of the catalytically active copper-ceria interfacial perimeter, *Nat. Catal.* 2 (4) (2019) 334–341.
- [13] J. Zhu, Y. Su, J. Chai, V. Muravev, N. Kosinov, E.J.M. Hensen, Mechanism and Nature of Active Sites for Methanol Synthesis from CO/CO₂ on Cu/CeO₂, *ACS Catal.* 10 (19) (2020) 11532–11544.
- [14] R. Burch, J.P. Breen, F.C. Meunier, A review of the selective reduction of NO_x with hydrocarbons under lean-burn conditions with non-zeolitic oxide and platinum group metal catalysts, *Appl. Catal., B* 39 (4) (2002) 283–303.
- [15] M. Carnegello, V.V.T. Doan-Nguyen, T.R. Gordon, R.E. Diaz, E.A. Stach, R.J. Gorte, et al., Control of Metal Nanocrystal Size Reveals Metal-Support Interface Role for Ceria Catalysts, *Science* 341 (6147) (2013) 771–773.
- [16] Y. Lin, Z. Wu, J. Wen, K. Yang, K.R. Poeppelmeier, et al., Adhesion and atomic structures of gold on ceria nanostructures: the role of surface structure and oxidation state of ceria supports, *Nano Lett.* 15 (8) (2015) 5375–5381.
- [17] A.M. Gaenzler, M. Casapu, F. Maurer, H. Stoermer, D. Gerthsen, G. Ferre, et al., Tuning the Pt/CeO₂ interface by in situ variation of the Pt particle size, *ACS Catal.* 8 (6) (2018) 4800–4811.
- [18] T.E. James, S.L. Hemmingson, T. Ito, C.T. Campbell, Energetics of Cu adsorption and adhesion onto reduced CeO₂(111) surfaces by calorimetry, *J. Phys. Chem. C* 119 (30) (2015) 17209–17217.
- [19] S.Y. Yao, W.Q. Xu, A.C. Johnston-Peck, F.Z. Zhao, Z.Y. Liu, S. Luo, et al., Morphological effects of the nanostructured ceria support on the activity and stability of CuO/CeO₂ catalysts for the water-gas shift reaction, *Phys. Chem. Chem., Phys.* 16 (32) (2014) 17183–17195.
- [20] D. Chen, Z. Su, W. Si, Y. Qu, X. Zhao, H. Liu, et al., Boosting CO catalytic oxidation performance via highly dispersed copper atomic clusters: regulated electron interaction and reaction pathways, *Environ. Sci. Technol.* 57 (7) (2023) 2928–2938.
- [21] Z. Hu, X. Liu, D. Meng, Y. Guo, Y. Guo, G. Lu, Effect of ceria crystal plane on the physicochemical and catalytic properties of Pd/Ceria for CO and propane oxidation, *ACS Catal.* 6 (4) (2016) 2265–2279.
- [22] K. Koizumi, K. Nobusada, M. Boero, The absence of a gap state and enhancement of the Mars-van Krevelen reaction on oxygen defective Cu/CeO₂ surfaces, *Phys. Chem. Chem., Phys.* 18 (30) (2016) 20708–20712.
- [23] Y.-G. Wang, D. Mei, J. Li, R. Rousseau, DFT+U study on the localized electronic states and their potential role during H₂O dissociation and CO oxidation processes on CeO₂(111) surface, *J. Phys. Chem. C* 117 (44) (2013) 23082–23089.
- [24] Y. Maimaiti, M. Nolan, S.D. Elliott, Reduction mechanisms of the CuO(111) surface through surface oxygen vacancy formation and hydrogen adsorption, *Phys. Chem. Chem. Phys.* 16 (7) (2014) 3036–3046.
- [25] D. Bucher, L.C.T. Pierce, J.A. McCammon, P.R.L. Markwick, On the use of accelerated molecular dynamics to enhance configurational sampling in ab initio simulations, *J. Chem. Theory Comput.* 7 (4) (2011) 890–897.
- [26] C. Scherer, F. Schmid, M. Letz, J. Horbach, Structure and dynamics of B₂O₃ melts and glasses: From ab initio to classical molecular dynamics simulations, *Comput. Mater. Sci.* 159 (2019) 73–85.
- [27] W. Ji, X. Chen, Q. Li, K. Lin, J. Deng, X. Xing, Insights into CO Oxidation in Cu/CeO₂ Catalysts: O₂ Activation at the Dual-Interfacial Sites, *Eur. J. Inorg. Chem.* 26 (10) (2023), e202200656.
- [28] W.-W. Wang, P.-P. Du, S.-H. Zou, H.-Y. He, R.-X. Wang, Z. Jin, et al., Highly dispersed copper oxide clusters as active species in copper-ceria catalyst for preferential oxidation of carbon monoxide, *ACS Catal.* 5 (4) (2015) 2088–2099.
- [29] Q. Wan, F. Wei, Y. Wang, F. Wang, L. Zhou, S. Lin, et al., Single atom detachment from Cu clusters, and diffusion and trapping on CeO₂(111): implications in Ostwald ripening and atomic redistribution, *Nanoscale* 10 (37) (2018) 17893–17901.
- [30] L. Nie, D. Mei, H. Xiong, B. Peng, Z. Ren, X.I.P. Hernandez, et al., Activation of surface lattice oxygen in single-atom Pt/CeO₂ for low-temperature CO oxidation, *Science* 358 (6369) (2017) 1419–1423.
- [31] K. Kim, J.D. Yoo, S. Lee, M. Bae, J. Bae, W. Jung, et al., A simple descriptor to rapidly screen CO oxidation activity on rare-earth metal-doped CeO₂: from experiment to first-principles, *ACS Appl. Mater. Interfaces* 9 (18) (2017) 15449–15458.
- [32] A.A. Alkhorri, K. Polychronopoulou, A. Belabbes, M.A. Jaoude, L.F. Vega, V. Sebastian, et al., Cu, Sm co-doping effect on the CO oxidation activity of CeO₂. A combined experimental and density functional study, *Appl. Surf. Sci.* 521 (2020), 146305.
- [33] H.J. Kim, M.G. Jang, D. Shin, J.W. Han, Design of ceria catalysts for low-temperature CO oxidation, *ChemCatChem* 12 (1) (2020) 11–26.
- [34] H.Y. Kim, H.M. Lee, G. Henkelman, CO oxidation mechanism on CeO₂-supported Au nanoparticles, *J. Am. Chem. Soc.* 134 (3) (2012) 1560–1570.
- [35] X. Wang, X. Du, S. Liu, G. Yang, Y. Chen, L. Zhang, et al., Understanding the deposition and reaction mechanism of ammonium bisulfate on a vanadia SCR catalyst: a combined DFT and experimental study, *Appl. Catal., B* 260 (2020), 118168.
- [36] T. Tang, X. Du, Y. Chen, J. Xue, K. Chen, X. Li, Study on the mechanism of selective catalytic reduction with propylene (C₃H₆-SCR) on the MnO_x-based catalysts by a doping experiment and DFT+U calculation, *J. Environ. Chem. Eng.* 11 (3) (2023), 109831.
- [37] R. Gui, J. Xiao, Y. Gao, Y. Li, T. Zhu, Q. Wang, Simultaneously achieving selective catalytic reduction of NO_x with NH₃ and catalytic oxidation of CO with O₂ over one finely optimized bifunctional catalyst Mn₂Cu₁Al₁O_x at low temperatures, *Appl. Catal., B* 306 (2022), 121104.
- [38] I. Nova, P. An, S. Liu, X. Zhang, D. Wang, Y. Yuan, et al., Reordering d orbital energies of single-site catalysts for CO₂ electroreduction, *Angew. Chem. Int. Ed.* 58 (36) (2019) 12711–12716.
- [39] Z. Gholami, G. Luo, F. Gholami, F. Yang, Recent advances in selective catalytic reduction of NO_x by carbon monoxide for flue gas cleaning process: a review, *Catal. Rev. Sci. Eng.* 63 (1) (2021) 68–119.
- [40] K. Khivantsev, N.R. Jaegers, H.A. Aleksandrov, I. Song, X.I. Pereira-Hernandez, M. H. Engelhard, et al., Single Ru(II) ions on ceria as a highly active catalyst for abatement of NO, *J. Am. Chem. Soc.* 145 (9) (2023) 5029–5040.
- [41] I. Nova, L. Lietti, P. Forzatti, F. Frola, F. Prinetti, G. Ghiotti, Reaction pathways in the reduction of NO_x species by CO over Pt-Ba/Al₂O₃: lean NO_x trap catalytic systems, *Top. Catal.* 52 (13–20) (2009) 1757–1761.
- [42] G.H. Major, N. Farley, P.M.A. Sherwood, M.R. Linford, J. Terry, V. Fernandez, et al., Practical guide for curve fitting in x-ray photoelectron spectroscopy, *J. Vac. Sci. Technol. A* 38 (6) (2020), 061203.
- [43] W. Zhu, S. Ndayiragije, X. Zuo, X. Zhang, G. Wang, X. Wang, ZIF-8-derived single-atom Cu and N co-coordinated porous carbon as bifunctional material for SMX removal, *J. Environ. Chem. Eng.* 10 (3) (2022), 107758.
- [44] G. Cao, N.A. Deskins, N. Yi, Carbon monoxide oxidation over copper and nitrogen modified titanium dioxide*, *Appl. Catal., B* 285 (2021), 119748.
- [45] S. Zhang, Z. Tian, Y. Ma, Y. Qu, Adsorption of molecules on defective CeO₂ for advanced catalysis, *ACS Catal.* 13 (7) (2023) 4629–4645.
- [46] P. Gawade, B. Bayram, A.-M.C. Alexander, Ozkan US. preferential oxidation of CO (PROX) over CoO_x/CeO₂ in hydrogen-rich streams: Effect of cobalt loading, *Appl. Catal., B* 128 (2012) 21–30.
- [47] Z. Wu, M. Li, S.H. Overbury, On the structure dependence of CO oxidation over CeO₂ nanocrystals with well-defined surface planes, *J. Catal.* 285 (1) (2012) 61–73.
- [48] P. Zang, J. Liu, Y. He, G. Zhang, G. Li, Y. Wang, et al., LDH-derived preparation of CuMgFe layered double oxides for NH₃-SCR and CO oxidation reactions: Performance study and synergistic mechanism, *Chem. Eng. J.* 446 (2022), 137414.
- [49] J. Li, J. Zhu, S. Fu, L. Tao, B. Chu, Q. Qin, et al., Insight into copper-cerium catalysts with different Cu valence states for CO-SCR and in-situ DRIFTS study on reaction mechanism, *Fuel* 339 (2023), 126962.
- [50] D. Gamarra, A.L. Cámara, M. Monte, S.B. Rasmussen, L.E. Chinchilla, A.B. Hungria, et al., Preferential oxidation of CO in excess H₂ over CuO/CeO₂ catalysts: Characterization and performance as a function of the exposed face present in the CeO₂ support, *Appl. Catal., B* 130–131 (2013) 224–238.
- [51] J. Guo, J. Xiao, R. Gui, Y. Gao, Q. Wang, Efficient simultaneous removal of NO_x and CO at low temperatures over integrated Mn₂Co₁O_x/iron mesh monolithic catalyst via NH₃-SCR coupling with CO oxidation reactions, *Chem. Eng. J.* 465 (2023), 142611.
- [52] J. Waikar, P. More, Low temperature oxidation of CO using alkali- and alkaline-earth metal-modified ceria-supported metal catalysts: a review, *Bull. Mater. Sci.* 44 (4) (2021) 263.
- [53] M. Piumetti, S. Bensaid, D. Fino, N. Russo, Nanostructured ceria-zirconia catalysts for CO oxidation: Study on surface properties and reactivity, *Appl. Catal., B* 197 (2016) 35–46.
- [54] M.A. Newton, D. Ferri, G. Smolentsev, V. Marchionni, M. Nachttegaal, Kinetic studies of the Pt carbonate-mediated, room-temperature oxidation of carbon monoxide by oxygen over Pt/Al₂O₃ using combined, time-resolved XAFS, DRIFTS, and mass spectrometry, *J. Am. Chem. Soc.* 138 (42) (2016) 13930–13940.
- [55] B. Liu, W. Li, W. Song, J. Liu, Carbonate-mediated Mars-van Krevelen mechanism for CO oxidation on cobalt-doped ceria catalysts: facet-dependence and coordination-dependence, *Phys. Chem. Chem. Phys.* 20 (23) (2018) 16045–16059.